A High-Performance WSe_2/*h*-BN Photodetector using a Triphenylphosphine (PPh_3)-Based n-Doping Technique

*Seo-Hyeon Jo, Dong-Ho Kang, Jaewoo Shim, Jaeho Jeon, Min Hwan Jeon, Gwangwe Yoo, Jinok Kim, Jaehyeong Lee, Geun Young Yeom, Sungjoo Lee, Hyun-Yong Yu, Changhwan Choi, and Jin-Hong Park**

Atomically thin transition metal dichalcogenides (TMDs) with a 2D semiconducting layered structure have recently come into the spotlight as suitable materials for next-generation electronics[1–4] and optoelectronics.[5–7] For electronic device applications, due to their excellent scalability to a monolayer based on its van der Waals epitaxial structure, TMDs have high immunity to a short channel effect, providing the possibility for achieving ultrascaled transistors with superior gate controllability.[8] In addition, a smooth surface without dangling bonds and thereby native oxides results in high carrier mobilities above 100 $cm^2\ V^{-1}\ s^{-1}$, even though the TMDs are sub-1 nm thick semiconductors.[1,9] Alternatively, TMDs also exhibit strong optical absorption (i.e., quantum efficiency: 45% for MoS_2[10] and 80% for WSe_2[11]) and ultrafast charge transfer (i.e., 5×10^{-14} s for the hole transport from MoS_2 to WS_2[12]), providing many opportunities for photodetection and photovoltaics. However, since one type of transistor can normally be fabricated on TMDs due to the Fermi-level pinning phenomenon between metals and TMDs[13,14] (i.e., n-channel for MoS_2 and p-channel for WSe_2), it is currently difficult to expand research regarding various TMD-based electronic and optoelectronic applications. In this light, recently reported works have focused on the fabrication of TMD devices that operate in the opposite way (p-channel in MoS_2 and n-channel in WSe_2) by reducing the high Schottky barriers at the metal-TMD contacts. Javey et al. reported the MoS_2 p-FET[15] and WSe_2 n-FET[16] by inserting a MoO_3 layer and applying a potassium doping technique at the metal-TMD junction, respectively. They also demonstrated the inverter circuit operation with complementary FETs fabricated on the same WSe_2 flake, where different contacts were formed (Pt/Au/Pd for p-FET and Au for n-FET). Another WSe_2 n-FET was achieved by Yu et al. through the low-work-function metal (Ag) contact and tetracyanoquinodimethane (F_4TCNQ) n-doping technique.[17] However, all researches currently remain at the level to accomplish simultaneously the different types of devices on one kind of TMDs. In particular, the performance of type-converted FET devices has not been clearly investigated in terms of optoelectronic devices.

Here, we report a high performance TMD photodetector with both a fast temporal photoresponse and a high responsivity that are in trade-off. This performance is achieved in a WSe_2-based FET fabricated on a hexagonal boron nitride (*h*-BN) layer by: i) converting the device type from a p- to n-channel and ii) precisely controlling the doping concentration of the WSe_2 layer through a triphenylphosphine (PPh_3)-based n-doping technique that is newly developed in this work. The phosphorus atoms in the PPh_3 molecules form lone pairs of electrons that enable the donation of electrons to the WSe_2 layer at level of 10^{11} cm^{-2}. First, we discuss the controllability of PPh_3 n-doping on WSe_2 with Raman spectroscopy and X-ray photoelectron spectroscopy (XPS). The effects of PPh_3 n-doping are then investigated on WSe_2-based FETs with different metal contacts (Ti and Pt) in terms of the performance of electronic (threshold voltage, on-current level, carrier concentration, and field-effect mobility) and optoelectronic (photoresponsivity and temporal photoresponse) devices. Finally, we further improve the photoresponsivity and temporal photoresponse performance of the PPh_3-doped WSe_2 photodetector by inserting the *h*-BN layer underneath the channel area and consequently suppressing the scattering phenomenon at the WSe_2/SiO_2 interface.

First, we prepared three different PPh_3 concentration solutions (2.5, 5.0, and 7.5 wt%) and WSe_2 samples, which were mechanically exfoliated onto a SiO_2/Si substrate by scotch-tape in order to investigate the effects of PPh_3 doping on the WSe_2 by Raman spectroscopy and XPS analyses. As shown in **Figure 1**a, two conventional Raman peaks (E^1_{2g} and A_{1g}) were observed near 250 and 260 cm^{-1} in the undoped WSe_2 sample (gray line), where the peaks indicate the in- and out-of-plane vibrations for bulk WSe_2, respectively.[18] The positions of the E^1_{2g} and A_{1g} Raman peaks were slightly blueshifted (dotted color lines) after performing the PPh_3 n-doping process on the WSe_2 films. We then extracted the peak shift values in each Raman peak before and after PPh_3 n-doping, and the values were plotted as a function of the PPh_3 concentrations in Figure 1b. For each

S.-H. Jo, D.-H. Kang, J. Shim, G. Yoo, J. Kim, Prof. J. Lee, Prof. J.-H. Park
School of Electronic and Electrical Engineering
Sungkyunkwan University
Suwon 440-746, South Korea
E-mail: jhpark9@skku.edu

J. Jeon, M. H. Jeon, Prof. G. Y. Yeom, Prof. S. Lee
SKKU Advanced Institute of Nanotechnology (SAINT)
Sungkyunkwan University
Suwon 440-746, South Korea

Prof. H.-Y. Yu
School of Electrical Engineering
Korea University
Seoul 136-701, South Korea

Prof. C. Choi
Division of Materials Science and Engineering
Hanyang University
Seoul 133-791, South Korea

DOI: 10.1002/adma.201600032

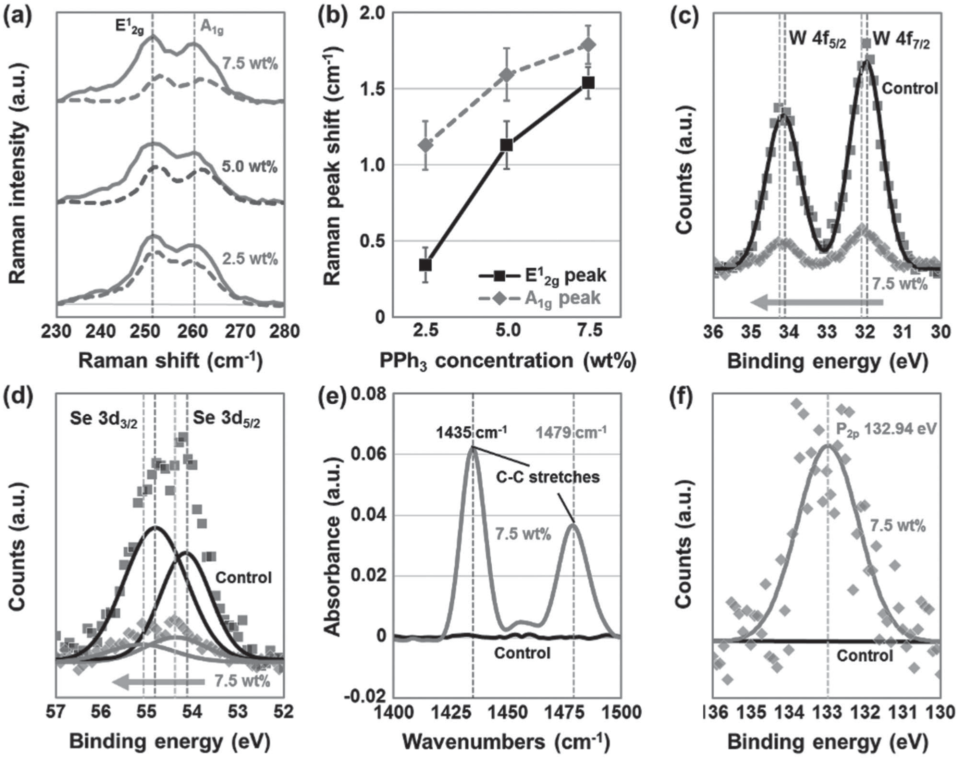

Figure 1. Characterization of the WSe_2 films before/after PPh_3 doping. a) Raman spectra of the control (solid line) and PPh_3-doped (dotted line) WSe_2 at different concentrations (2.5, 5.0, and 7.5 wt%). b) Extracted Raman peak shift values of WSe_2 doped by PPh_3 as a function of the PPh_3 concentration. XPS analysis of WSe_2 before and after 7.5 wt% PPh_3 doping with binding energy peaks of: c) W $4f_{5/2}$ and $4f_{7/2}$ and d) Se $3d_{3/2}$ and $3d_{5/2}$ electrons. e,f) C–C stretch peaks and P 2p electron binding energy peaks appeared in FTIR (e) and XPS (f) spectra after 7.5 wt% PPh_3 doping.

doping condition, eight different samples were prepared, and the Raman measurements were performed at three different points in each sample. As shown in Figure 1b, blueshifting of the E^1_{2g} and A_{1g} peaks was observed in the ranges of 0.34–1.54 and 1.13–1.79 cm^{-1}, respectively. The blueshifting (for E^1_{2g} and A_{1g} peaks) became clearer as the PPh_3 concentration increased. In previous Raman studies on WSe_2, an erratic Raman peak shift was reported after the p-doping process by various materials: blueshift by octadecyltrichlorosilane,[19] redshift by Au nanoparticles,[20] and no-shift by NO_x.[21] Because it was not obvious that Raman analysis could confirm the type of doped WSe_2, we then performed XPS measurements on the undoped/PPh_3-doped WSe_2 films. Figure 1c,d shows the binding energy peaks of W 4f and Se 3d before and after the 7.5 wt% PPh_3 n-doping on the WSe_2 film. After the PPh_3 n-doping, the W 4f and Se 3d peaks were upshifted by 0.08 and 0.3 eV, respectively, indicating that the Fermi level of WSe_2 moved toward the conduction band edge (n-type doping phenomenon).[16,22] The previous XPS analysis of potassium n-doped WSe_2 reported by Fang et al. also showed an up-shift (≈0.4 eV) of the electron binding energy peaks.[16] In addition, FT-IR and XPS analyses were used to verify the characteristics of the PPh_3 layers on the WSe_2 flakes. As shown in Figure 1e, two conventional C–C stretch peaks were observed at 1435 cm^{-1} and 1479 cm^{-1}, which indicate phenyl groups (C_6H_5–) in the PPh_3 atomic structure. The existence of phosphorus atoms in the PPh_3 was also confirmed through the XPS spectra of the phosphates (P 2p peak at 132.94 eV) in Figure 1f.

In order to investigate the PPh_3 n-doping effects on the electrical performance of WSe_2 FETs, we then fabricated back-gated WSe_2 FET devices with two different metal contacts (titanium and platinum) and performed current–voltage measurements (I_D–V_G and I_D–V_D) in air. **Figure 2**a,b shows the schematic illustration, the optical image of the PPh_3-treated WSe_2 device (both the channel length and width are 5 µm), and the detailed description of the n-doping mechanism at the PPh_3/WSe_2 interface. As described in Figure 2b, when the PPh_3 layer was coated on the WSe_2 devices, the electron lone pair of PPh_3 is expected to induce a negative charge transfer phenomenon from PPh_3 to WSe_2, thereby shifting up the Fermi level of the WSe_2. This phenomenon consequently increases an effective hole barrier height at the Pt/WSe_2 junction and decreases the hole injection probability from the source (Pt) to the channel (WSe_2). In contrast, the up-shift of the WSe_2 Fermi level by the PPh_3 n-doping seems to reduce the effective electron barrier height at the Ti–WSe_2 junction, increasing the electron injection probability from Ti to the WSe_2 channel. As shown in Figure 2c–j, we then extracted various electrical parameters (ΔV_{TH}, Δn, μ_{FE}, and I_{on}) and evaluated the PPh_3-doped Ti– and Pt–WSe_2 devices with applied PPh_3 concentrations of 2.5, 5.0, and 7.5 wt%. For the extraction, the field-effect mobility formula $\mu_{FE} = L/(WV_DC_{OX}) \times (\partial I_D/\partial V_G)$ and 2D sheet doping concentration formula n (or p) $= I_DL/qW\mu V_D$ were used, where q is the electron charge, L and W are the length and width of the channel, respectively, and the gate oxide capacitance per unit area (C_{OX}) is $\varepsilon_{OX} \times \varepsilon_0/t_{OX}$. μ_{FE} was calculated at $V_{GS} - V_{TH} = 0$ V,

DOI: 10.1002/adma.201600032

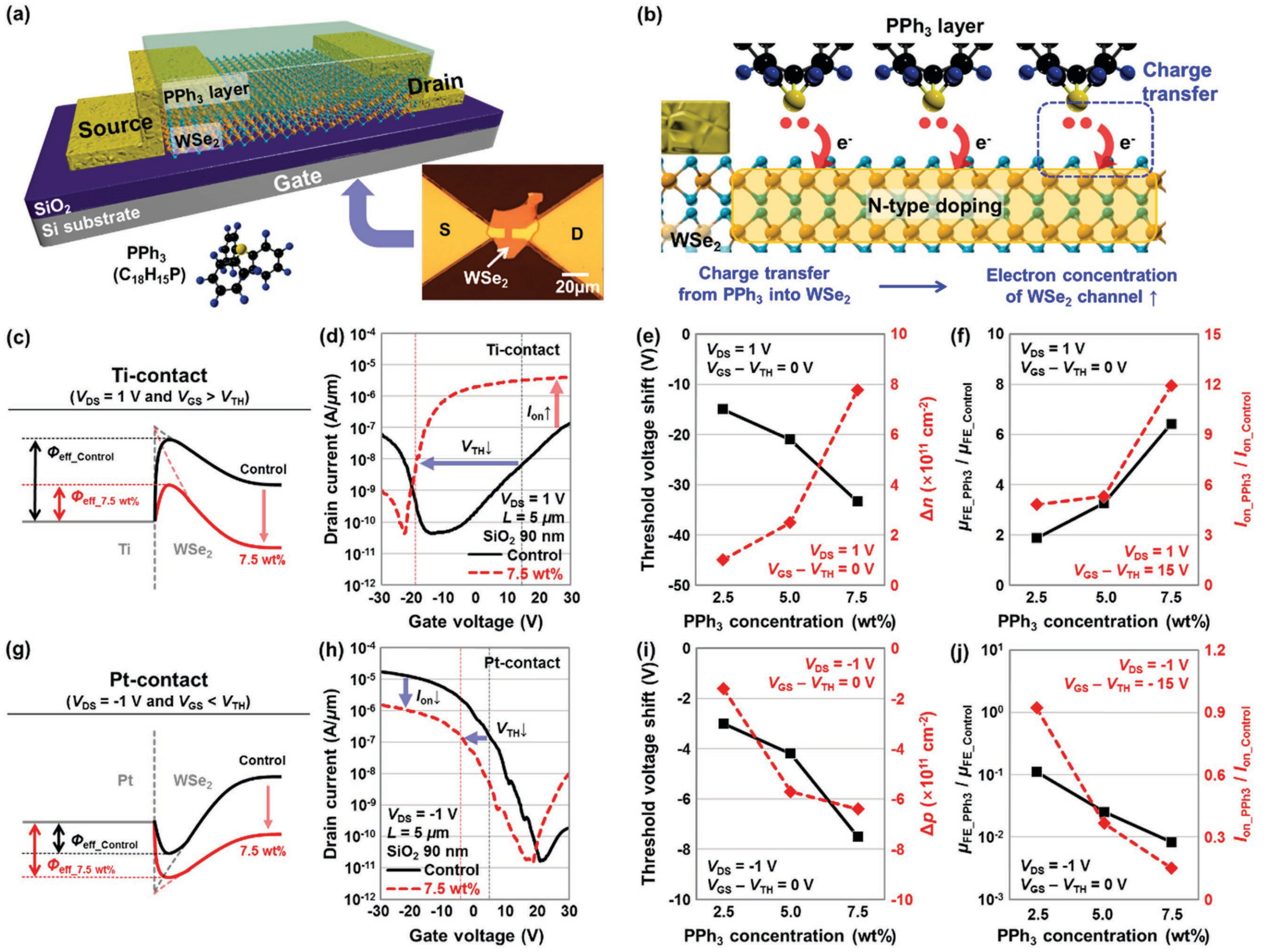

Figure 2. Electrical characterization of PPh$_3$-doped Ti– and Pt–WSe$_2$ transistors. a) Schematic diagram and optical image of back-gated (90-nm thick SiO$_2$ gate dielectric) WSe$_2$ transistor device doped by PPh$_3$. b) Descriptive diagram for the n-doping mechanism of PPh$_3$ at the PPh$_3$/WSe$_2$ interface. c,g) Energy-band diagram of Ti-WSe$_2$ (c), Pt–WSe$_2$ (g) junctions at on-state before and after 7.5 wt% PPh$_3$ doping. d,h) I_D–V_G characteristics of control (black solid line) and 7.5 wt% PPh$_3$-doped (red dotted line) WSe$_2$ transistors (L = 5 μm) with Ti-contact (V_{DS} = 1 V) (d) or Pt-contact (V_{DS} = −1 V) (h). e,i) The extracted threshold voltage shifts ($\Delta V_{TH} = V_{TH\_PPh3} - V_{TH\_Control}$) and carrier concentration differences ($\Delta n = n_{PPh3} - n_{Control}$ and $\Delta p = p_{PPh3} - p_{Control}$) at $V_{GS} = V_{TH}$ in the WSe$_2$ transistors with Ti-contact (V_{DS} = 1 V) (e) or Pt-contact (V_{DS} = −1 V) (i). f,j) The extracted field-effect mobility ratio (μ_{FE} ratio = $\mu_{FE\_PPh3}/\mu_{FE\_Control}$) at $V_{GS} = V_{TH}$ and on-current ratio (I_{on} ratio = $I_{on\_PPh3}/I_{on\_Control}$) at $V_{GS} = V_{TH}$ + 15 V (n-FET) and $V_{GS} = V_{TH}$ – 15 V (*p*-FET) in WSe$_2$ transistors with Ti-contact (V_{DS} = 1 V) (f) or Pt-contact (V_{DS} = −1 V) (j).

and I_{on} was extracted at $V_{GS} - V_{TH}$ = 15 V (Ti-contacted device) and $V_{GS} - V_{TH}$ = −15 V (Pt-contacted device). We note that the contact resistance was not clearly excluded in the μ_{FE} calculation so that the extracted μ_{FE} values were dependent on the contact resistance (also, carrier injection at the metal–TMD junction interface) and slightly underestimated due to the considerable contact resistance.[23] Figure 2c,g shows the energy-band diagrams of the Ti- and Pt–WSe$_2$ junctions at on-state before/after the PPh$_3$ n-doping process by various concentrations of PPh$_3$ solutions. In the case of the Ti–WSe$_2$ junctions (Figure 2c), the electron carrier injection from Ti to WSe$_2$ is expected to improve as the PPh$_3$ concentration increases due to the reduction in effective electron barrier height. As a result, the extracted V_{TH} value shifted from 14.1 to −19.2 V and the on-current (at $V_{GS} - V_{TH}$ = 15 V) increased from 1.24 × 10^{-7} to 1.47 × 10^{-6} A μm^{-1} after 7.5 wt% PPh$_3$ doping, as shown in Figure 2d. The corresponding I_D–V_D characteristic curves are shown in Figure S1 in the Supporting Information, which also indicates that the PPh$_3$-doped Ti-contacted WSe$_2$ device was successfully type-converted to the n-channel device. Figure 2e,f shows the electrical parameters (V_{TH}, Δ*n*, μ_{FE}, and I_{on}) as a function of the PPh$_3$ concentrations, which were extracted from the Ti-contacted devices. When the PPh$_3$ concentration increased, ΔV_{TH} decreased from −15 to −33.3 V and Δ*n* increased from 1.02 × 10^{11} to 7.77 × 10^{11} cm^{-2}. These Δ*n* values were observed in the nondegenerate level, which are very similar to the levels of the previously reported OTS p-doping[19] (≈2.3 × 10^{11} cm^{-2}) or Cs$_2$CO$_3$ n-doping[24] (≈3.5 × 10^{11} cm^{-2}). Additionally, as shown in Figure 2f, μ_{FE} and I_{on} were respectively improved from 1.88 to 6.42 (μ_{FE} ratio) and from 4.81 to 11.9 (I_{on} ratio) with increasing PPh$_3$ concentration, where the highest μ_{FE} and I_{on} values were 18.9 cm^2 V^{-1} s^{-1} and 4.0 × 10^{-6} A μm^{-1}, respectively, in the 7.5 wt% PPh$_3$-doped Ti–WSe$_2$ device. This enhancement in μ_{FE} and I_{on} seems attributable to the increase in the electron carrier

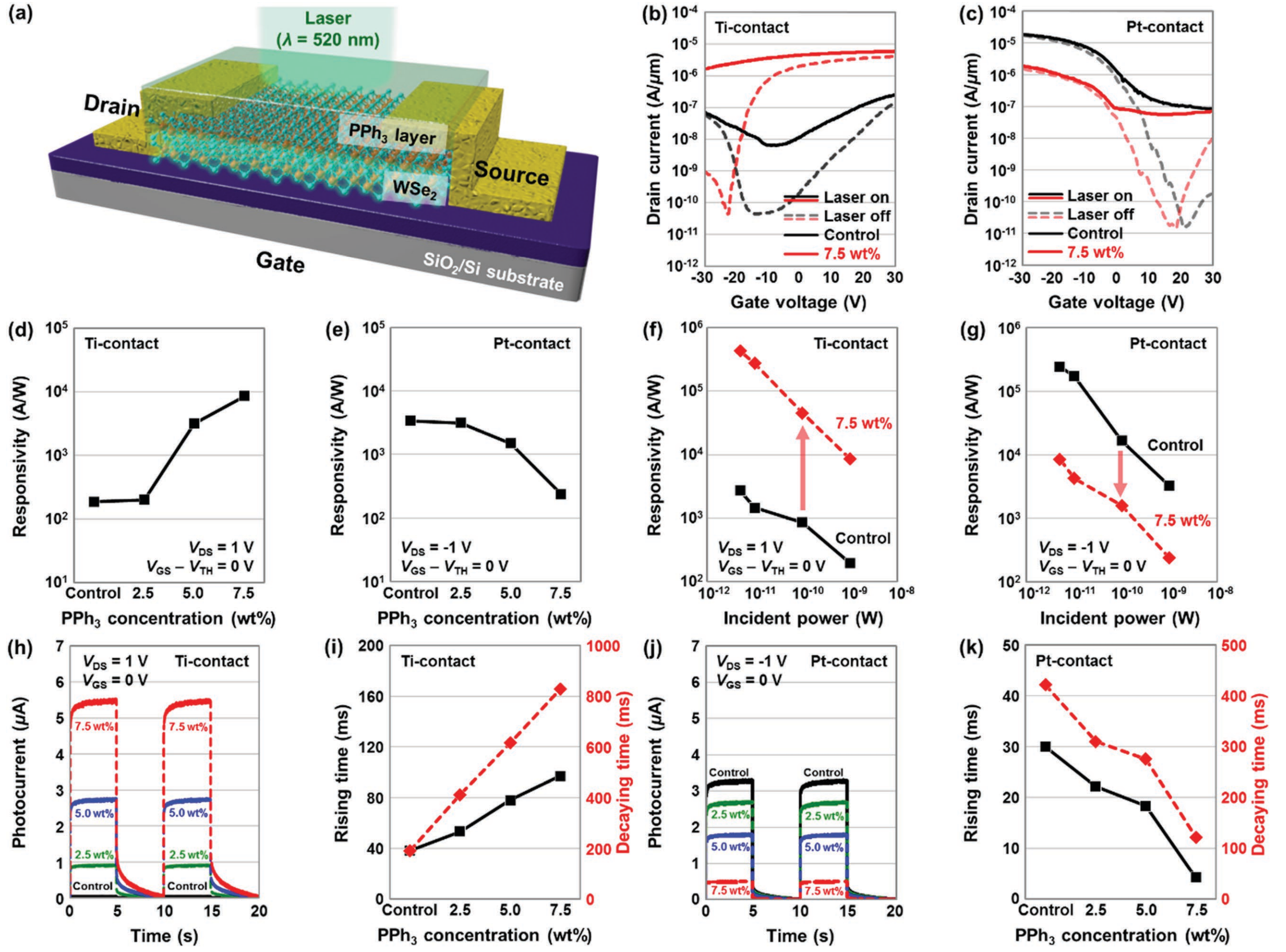

Figure 3. Optoelectronic characterization of PPh$_3$-doped Ti– and Pt–WSe$_2$ photodetectors. a) Schematic of the PPh$_3$-doped WSe$_2$ photodetector under laser illumination ($P_{\text{Light}} = 4$ mW cm^{-2} and $\lambda = 520$ nm). b,c) I_D–V_G characteristics of the control (black) and PPh$_3$-doped (red) photodetectors under both dark (dotted line) and illuminated (solid line) conditions with Ti-contact ($V_{DS} = 1$ V) (b) or Pt-contact ($V_{DS} = -1$ V) (c). d,e) Photoresponsivity as a function of the PPh$_3$ doping concentration, which was extracted at $V_{GS} = V_{TH}$ in the photodetectors with Ti-contact ($V_{DS} = 1$ V) (d) or Pt-contact ($V_{DS} = -1$ V) (e). f,g) Photoresponsivity as a function of incident laser power (5, 10, 100, and 1000 pW) was extracted at $V_{GS} = V_{TH}$ before and after 7.5 wt% PPh$_3$-doping in the WSe$_2$ photodetectors with Ti-contact ($V_{DS} = 1$ V) (f) or Pt-contact ($V_{DS} = -1$ V) (g). h-k) The temporal photoresponse characteristics and rising/decaying times of the photodetectors were obtained at $V_{GS} = 0$ V with Ti-contact ($V_{DS} = 1$ V) (h,i) or and Pt-contact ($V_{DS} = -1$ V) (j,k), respectively.

injection probability as the PPh$_3$ concentration increases. Compared to the Ti-contacted WSe$_2$ devices, the PPh$_3$ n-doping oppositely influenced the electrical characteristics in the Pt-contacted WSe$_2$ devices. As shown in Figure 2g, the hole carrier injection from Pt to WSe$_2$ seems to deteriorate as the PPh$_3$ concentration increases, due to the increase in the effective hole barrier height at the Pt–WSe$_2$ junction. Consequently, in the 7.5 wt% PPh$_3$-doped Pt-contacted devices, V_{TH} shifted from 4.5 to −3 V and the on-current (at $V_{GS} - V_{TH} = -15$ V) decreased from 5.84×10^{-6} to 8.78×10^{-7} A μm^{-1} (**Figure** 3h). We also extracted and compared the electrical parameters with varying PPh$_3$ concentration, as shown in Figure 2i,j. Although the extracted ΔV_{TH} and Δp values were similarly changed as a function of the PPh$_3$ concentration like the case of the Ti-contacted devices showing n-doping behaviors (ΔV_{TH}: −3.0 → −7.5 V and Δp: $-1.6 \times 10^{11} \rightarrow -6.4 \times 10^{11}$ cm^{-2} in Figure 2e), the μ_{FE} and I_{on} ratio values were respectively reduced from 1.11×10^{-1} to 8.26×10^{-3} cm^{-2} and from 9.21×10^{-1} to 1.50×10^{-1} A μm^{-1} as the PPh$_3$ concentration increased. In contrast to the performance enhancement in the Ti-contacted devices, the electrical performance of the Pt-contacted devices degraded with increasing PPh$_3$ concentration. This degradation can also be explained by the decrease in the hole carrier injection probability, owing to the increase in effective hole barrier height at the Pt–WSe$_2$ junction with increasing PPh$_3$ concentration. We also confirmed the controllability of PPh$_3$ n-doping in both Ti- and Pt-contacted WSe$_2$ devices by adjusting the PPh$_3$ concentration, which is consistent with the Raman analysis (Figure 1a,b). In addition, we investigated the stability of the PPh$_3$ doping effects on Ti- and Pt-contacted WSe$_2$ devices with various concentrations (2.5, 5.0, and 7.5 wt%, Figure S2, Supporting Information). After 24 h in air, the threshold voltage shifts of 2.5 wt% and 5.0 wt% PPh$_3$-doped samples decreased ≈10.1–53.1% in Ti–WSe$_2$ and 22.6–33.9% in Pt–WSe$_2$, respectively. In particular, after 7.5 wt% PPh$_3$ doping, very small threshold voltage shifts were observed after 192 h in air (3.83% and 2.73% in the Ti– and

DOI: 10.1002/adma.201600032

Pt–WSe_2 samples, respectively), indicating that the 7.5 wt% PPh_3-doped FET device was remarkably stable compared to the devices doped by other techniques, such as OTS[19] (ΔV_{TH}: 22.3% after 120 h).

Next, we investigated the PPh_3 n-doping effects on the optoelectronic performance of WSe_2 photodetectors by performing electrical measurements in air under dark and laser illuminated conditions ($\lambda = 520$ nm). Figure 3a shows the schematic illustration of the PPh_3-doped WSe_2 photodetector with different contact electrodes (Ti and Pt). When the PPh_3 layer was applied to the Ti-contacted devices, the contact resistance decreased because of the reduction in the effective electron-injection barrier height. This eventually appears to improve the photocurrent by increasing the electric field at the WSe_2 region, as shown in Figure 3b. After the Ti-contacted WSe_2 device was doped with 7.5 wt% PPh_3, the photocurrent increased from 5.87×10^{-8} to 2.59×10^{-6} A µm^{-1}, which was extracted at $V_{GS} = V_{TH}$. In contrast, the photocurrent of the Pt-contacted WSe_2 photodetector decreased after the PPh_3 n-doping (Figure 3c) due to the reduced photocarrier collection at the WSe_2 region by the increase in the Pt–WSe_2 contact resistance. In order to investigate the detailed PPh_3 doping effects on the WSe_2 photodetectors, the photoresponsivity ($R = I_{Photo}/P_{Light}$) was then extracted before and after the PPh_3*n*-doping with different concentrations (2.5, 5.0, and 7.5 wt%). Here, the generated photocurrent (I_{Photo}) is $I_{Laser\_on} - I_{Laser\_off}$, and P_{Light} is the total incident laser power. The photoresponsivity extractions were performed when V_{GS} was equal to V_{TH} (Figure S3, Supporting Information). In the case of the control devices (undoped WSe_2 photodetector), the photoresponsivity values were ≈1.86×10^2 A W^{-1} (Ti-contacted devices) and 3.39×10^3 A W^{-1} (Pt-contacted devices). Because of the opposite-behavior in the contact resistances at source–WSe_2 junctions by PPh_3 n-doping, specifically, a decrease (Ti-contacted devices) and an increase (Pt-contacted device) in contact resistance (above Figure 2), the photocarrier collection is expected to be suppressed and enhanced in the Ti- and Pt-contacted devices, respectively. Higher contact resistance at the metal–TMD junction interface seems to reduce the effective electric field in the TMD region. When the PPh_3 layer doped the Ti-contacted photodetector, an increasing trend in the photoresponsivity was observed as a function of the PPh_3 concentration from 1.86×10^2 (control) to 8.63×10^3 A W^{-1} (7.5 wt%). Alternatively, the photoresponsivity of the doped Pt-contacted devices decreased as the PPh_3 concentration increased ($3.39 \times 10^3 \rightarrow 2.37 \times 10^2$ A W^{-1} at 7.5 wt%).

Figure 3f–k shows the additional analyses of the PPh_3-doped WSe_2 photodetectors, which are related to the total incident power (f–g) and temporal photoresponse (h–k). According to previous report,[25] the photoresponsivity of the photodetectors increased as an inverse exponential function of the incident power of the laser because the scattering effect among the photogenerated carriers was suppressed under low-power laser illumination. The photocurrents were measured after exposing the lasers with different incident powers (5, 10, 100, and 1000 pW) and then the photoresponsivity values were extracted as a function of the incident power. In the case of Ti-contacted devices (Figure 3f), the photoresponsivity increased by a factor of 13.81 (control device) and 49.91 (7.5 wt% PPh_3-doped device) as the incident power decreased, where the maximum photoresponsivity was 4.31×10^5 A W^{-1} (under 5 pW in the 7.5 wt% PPh_3-doped device). A similar improvement in photoresponsivity by reducing the incident power of the laser was also observed in the Pt-contacted devices (Figure 3g), but the photoresponsivity values of the PPh_3-doped devices were much less than those of the Ti-contacted devices due to the negative effect of PPh_3 doping on the Pt–WSe_2 contact ($2.43 \times 10^5 \rightarrow 8.52 \times 10^3$ A W^{-1}, under 5 pW laser). In addition, the temporal photoresponse in the PPh_3-doped WSe_2 photodetectors was measured with laser-switching cycles of 5 s. The extraction method for the rising and decaying times is explained in detail in Figure S4 in the Supporting Information. Figure 3h,j presents the temporal photoresponse curves of the Ti- and Pt-contacted photodetectors doped by various concentrations of PPh_3. In the case of Ti-contacted devices, the photoresponse times increased (τ_r: 38.2 → 97 ms and τ_d: 191 → 827 ms) as the PPh_3 concentration increased. Alternatively, an improvement in the rising and decaying times was observed in the PPh_3-doped and Pt-contacted devices (τ_r: 30 → 4.2 ms and τ_d: 422 → 122 ms). This conflicting photoresponse can be explained by the different variations in the depletion widths of the Ti– and Pt–WSe_2 junctions by PPh_3-doping. The depletion width of the Ti–WSe_2 junction is expected to narrow as the PPh_3 concentration increases, as opposed to the expanded depletion width at the Pt–WSe_2 junction. Because the narrowed depletion width makes it difficult to collect the photogenerated carriers in the WSe_2 region, the photoresponse (rising and decaying times) of the PPh_3-doped and Ti-contacted photodetectors becomes slower than the undoped devices, which is opposite to the Pt–WSe_2 devices which show a faster photoresponse after the PPh_3 n-doping.

By converting the WSe_2 device type (p- to n-channel) through PPh_3 n-doping and Ti contact formation, we could achieve a high photoresponsivity that is similar to (or slightly greater than) that of the Pt–WSe_2 photodetector (Ti–WSe_2: 4.31×10^5 A W^{-1} and Pt–WSe_2: 2.43×10^5 A W^{-1}), but the temporal photoresponse times (τ_r: 97 ms and τ_d: 827 ms) were 2–3 times degraded compared to the Pt–WSe_2 device (τ_r: 30 ms and τ_d: 422 ms). Therefore, in order to recover the degraded temporal photoresponse time of the photodetector and eventually make the n-channel device performance comparable to the p-channel WSe_2 photodetector, an *h*-BN layer was employed to the Ti-contacted n-channel WSe_2 photodetector. Because the *h*-BN layer provides a charge-free environment for the channel region, it can enhance the carrier mobility of the TMD FET devices by inserting at TMD/SiO_2 interface[26,27] or encapsulating the TMD surfaces.[28,29] **Figure 4**a shows the schematic diagrams and the optical microscopy images of the PPh_3-doped WSe_2 device with *h*-BN between the WSe_2 and SiO_2 layers. Here, we used an inverse transfer technique for fabricating the WSe_2/*h*-BN heterostructure-based device (Figure S5, Supporting Information) to achieve a clean WSe_2/*h*-BN interface. By inserting *h*-BN between the WSe_2 channel and the SiO_2 gate dielectric, as shown in Figure 4b, the photoresponsivity of the PPh_3-doped Ti-contacted WSe_2 photodetector was increased by a factor of 1.9 ($6.67 \times 10^5 \rightarrow 1.27 \times 10^6$ A W^{-1} under 5 pW laser exposure). Here, we compared the maximum photoresponsivity values obtained in the same range of gate voltage (between −30 V and 30 V). For reference, this increasing trend in photoresponsivity after *h*-BN insertion will be still valid even after

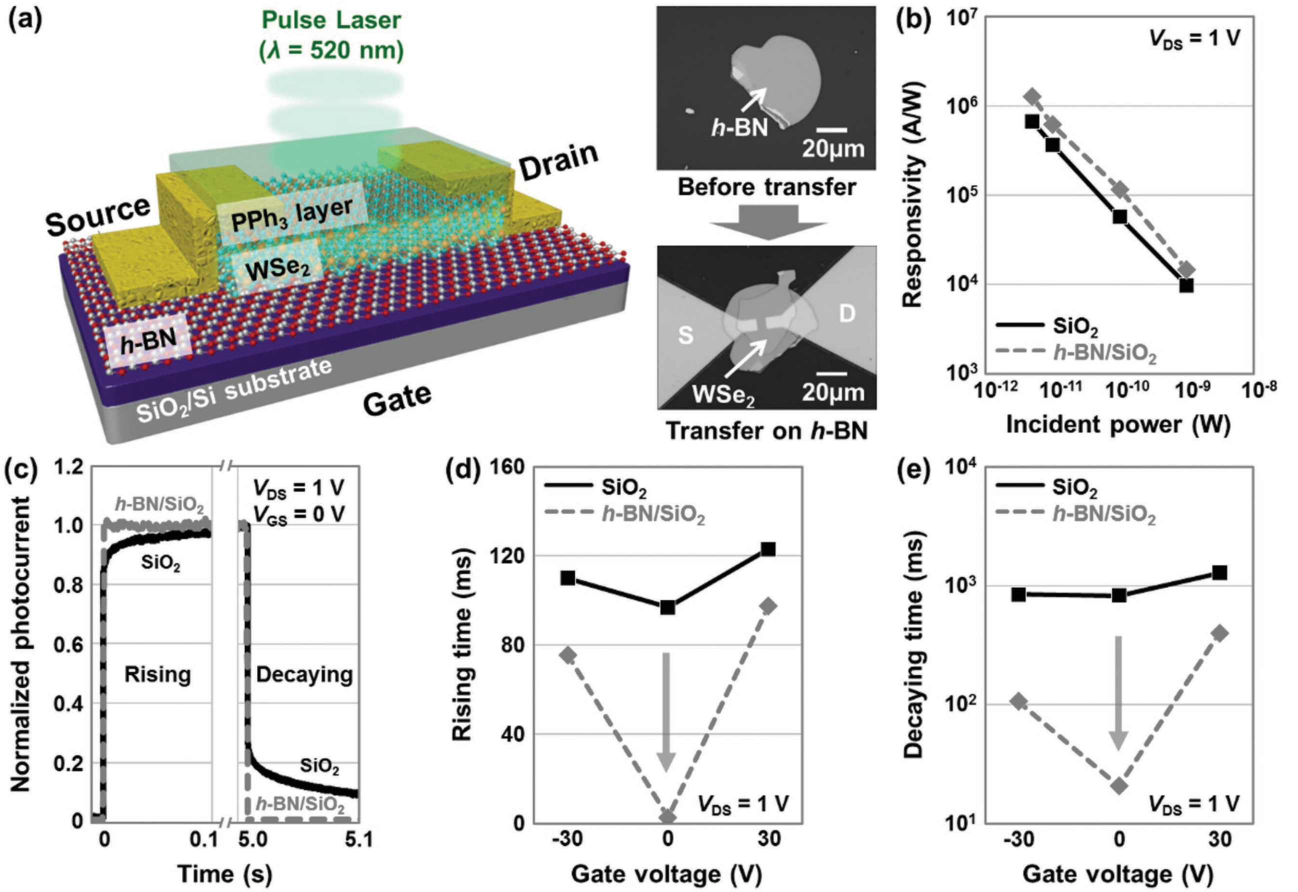

Figure 4. Characterization of PPh_3-doped Ti–WSe_2/*h*-BN photodetectors. a) Schematic diagram and optical images (before and after transfer) of *h*-BN inserted into the Ti-contacted WSe_2 photodetector that was doped by 7.5 wt% PPh_3. b) Extracted photoresponsivity as a function of the incident laser power (5, 10, 100, and 1000 pW) before and after transferring to the *h*-BN/SiO_2 substrate. c) Normalized temporal photoresponse curves at the rising and decaying edges. d,e) Rising (d) and decaying (e) times of the photodetector as a function of the gate voltage (V_G = –30, 0, and 30 V), where the drain voltage (V_{DS}) was 1 V.

equalizing the gate capacitances because the smaller vertical electric field in the *h*-BN-inserted photodetectors (compared to the control devices) is expected to induce weaker photoresponsivity. This improvement can be attributed to the increased carrier mobility (from 18.9 $cm^2\ V^{-1}\ s^{-1}$ before the insertion of *h*-BN to 25.6 $cm^2\ V^{-1}\ s^{-1}$ after the insertion) and the subsequently enhanced carrier collection, which were obtained by separating the WSe_2 channel region from the charged surface of SiO_2.[26] As the incident laser power was reduced from 1000 to 5 pW, the photoresponsivity increased by approximately two orders of magnitude as a function of the inverse of the power, due to the suppressed scattering probability of the photogenerated carriers. In addition, the temporal responses of the PPh_3-doped Ti-contacted WSe_2 photodetectors with and without an *h*-BN layer were investigated. The temporal photoresponse curves in Figure 4c (V_{DS} = 1 V and V_{GS} = 0 V) clearly show that the rising and decaying time were improved after inserting the *h*-BN layer. As shown in the extracted rising (Figure 4d) and decaying (Figure 4e) time values, enhanced temporal responses were observed in all ranges of the applied gate voltage (between –30 V and 30 V). This enhancement may also be caused by the improved carrier mobility via insertion of the *h*-BN layer because high mobility will boost the transporting speed of the photocarriers. The shortest temporal response time was observed at V_G = 0 V, and the rising and decaying times were respectively enhanced from 97 to 2.8 ms and 827 to 20.8 ms by applying the *h*-BN layer, where the improved values were much shorter than those of Pt-contacted WSe_2 control device (τ_r: 30 ms and τ_d: 422 ms). By applying the *h*-BN layer to the PPh_3-doped Ti-contacted WSe_2 photodetector, we successfully recovered the temporal photoresponse time, where the obtained photoresponse time in milliseconds was similar to the value (1.8–2.0 ms) of the photodetector fabricated on MoS_2 by using a ferroelectric material, P(VDF-TrFE), as a gate insulator.[30] For reference, when a 2D material-based photodetector was fabricated in vertical hybrid structure consisting of $GaTe_xSe_{1-x}$ and Si, its rising and decaying times were relatively lower as much as 130 and 70 µs, respectively.[31] In addition, we confirmed that the temporal photoresponse time was affected by an applied gate voltage bias in all photodetectors. According to Figure 4d,e and Figure S6 (Supporting Information), the rising and decaying times were degraded at V_G = ±30 V compared to the zero gate bias (V_G = 0 V). This phenomenon seems to be caused by the electron/hole carrier accumulation that

DOI: 10.1002/adma.201600032

is formed when a positive or negative gate voltage is applied, which consequently occurs as a carrier scattering effect in the WSe_2 channel region and thereby reduces the mobility of the photogenerated carriers.

In conclusion, we demonstrated a WSe_2-based photodetector with high responsivity and fast switching speed through: i) FET-type conversion (n- to p-channel) via a PPh_3 n-doping technique, and ii) *h*-BN insertion underneath the WSe_2 channel. Especially, the obtained maximum photoresponsivity was a record value up to present, compared to other single TMD material-based photodetectors. The n-doping originated from the electron transfer phenomenon from the lone pair of phosphorus atoms in PPh_3. The achieved n-doping concentration (Δn and Δp) on the WSe_2 films was in a nondegenerate regime, presenting values between 1.02×10^{11} cm^{-2} and 7.77×10^{11} cm^{-2} (Δn in Ti-contacted WSe_2 device) and between -1.61×10^{11} cm^{-2} and -6.4×10^{11} cm^{-2} (Δp in Pt-contacted WSe_2 device). We also investigated the PPh_3 doping effects in terms of the performance of WSe_2-based electronic and optoelectronic devices (V_{TH}, μ_{FE}, I_{on}, photoresponsivity, and temporal photoresponse) by adjusting the doping concentrations. By forming Ti contacts and performing a 7.5 wt% PPh_3 n-doping process, we completely converted the WSe_2 FET from a p- to n-channel, and also achieved a comparable performance to that of the Pt-contacted WSe_2 p-FET device. In the case of the photodetector, the photoresponsivity increased ($2.70 \times 10^3 \rightarrow 4.31 \times 10^5$ A W^{-1} under 5 pW laser exposure), but the temporal photoresponse deteriorated (τ_r: 38.2 → 97 ms and τ_d: 191 → 827 ms) after 7.5 wt% PPh_3 n-doping and Ti contact formation. The poor temporal photoresponse was then recovered by applying the *h*-BN layer at the WSe_2/SiO_2 interface and eventually suppressing the carrier scattering at the channel region. As a result, the maximum photoresponsivity was enhanced from 6.67×10^5 to 1.27×10^6 A W^{-1} under 5 pW laser exposure, and the rising and decaying times were also recovered from 97 to 2.8 ms and from 827 to 20.8 ms, respectively, which are comparable to or better than the performance of the Pt-contacted WSe_2 photodetector. Furthermore, we confirmed that the PPh_3 doping was very stable in air with only 3.83% (Ti contact) and 2.73% (Pt contact) variations in V_{TH} observed for 192 h in the case of the 7.5 wt% PPh_3-doped WSe_2 devices.

Experimental Section

PPh_3 n-Doping of WSe_2: For preparing the PPh_3 solutions, different amounts of triphenylphosphine (0.25, 0.50, and 0.75 g) were respectively dissolved in various amounts of toluene (9.75, 9.50, and 9.25 g) to produce doping solutions with various concentrations of PPh_3, respectively, named as PPh_3 2.5, 5.0, and 7.5 wt%. For doping WSe_2, the PPh_3 solution was spin-coated on the prepared WSe_2 samples at 1000 rpm for 30 s (5 s acceleration). The samples were then annealed at 150 °C for 10 min to remove the remaining solvent.

Raman, XPS, and FT-IR Analyses of PPh_3-Doped WSe_2: The characteristics of the WSe_2 (which was mechanically exfoliated and transferred to the SiO_2/Si substrate) were investigated by Raman spectroscopy (Alpha300 M+, WITec), XPS (ESCA200, VG Microtech Inc.), and FTIR (IFS-66/S, Bruker) before and after PPh_3 *n*-doping. Raman spectroscopy with an excitation wavelength of 532 nm was used with a laser beam size of 0.7–0.9 µm and an instrumental spectral resolution less than 0.9 cm^{-1}. The integration time was 5 s and a spectrometer with 1800 grooves mm^{-1} was employed for the test. A Mg K$_\alpha$ twin-anode source was used for the XPS measurement, where the X-ray incident angle was 0°. The FTIR spectral range was between 4000 and 20 cm^{-1}, the scan rate was 110 scans s^{-1}, and the resolution was greater than 0.1 cm^{-1}.

Fabrication of PPh_3-Doped WSe_2 Electronic and Optoelectronic Devices: The WSe_2 flake was mechanically exfoliated and transferred to the 90 nm thick, SiO_2 oxidized, heavily boron-doped Si substrate via adhesive tape (224SPV, Nitto). The remaining adhesive tape residue was removed by immersing the samples in an acetone bath for 1 h. For the fabrication of the back-gated WSe_2 devices (transistors and photodetectors), source/drain electrode regions (channel length and width were 5 µm) were patterned on the $WSe_2/SiO_2/Si$ samples by an optical lithography process, followed by 10 nm thick Ti (for *n*-type FET) or Pt (for p-type FET) and 50-nm thick Au deposition processes via an e-beam evaporator. Additionally, the fabricated WSe_2 devices were transferred to the *h*-BN/SiO_2/Si substrate by an inverse transfer method using poly(methyl methacrylate) (PMMA) and poly(vinyl alcohol) (PVA) supporting layers (Figure S5, Supporting Information).

Electrical Characterization of the PPh_3-Doped WSe_2 Electronic Device: The fabricated devices were electrically analyzed through electrical measurements (I_D–V_G and I_D–V_D) by an HP 4155A semiconductor parameter analyzer. The threshold voltage (V_{TH}), carrier concentration (n or p), and field-effect mobility (μ_{FE}) were calculated from the measured data. Here, all drain currents (I_D) were normalized by the channel width (W). The carrier concentration and field-effect mobility were respectively extracted using $n \text{ (or p)} = I_D L / qW\mu V_D$ and $\mu_{FE} = L/(WV_D C_{OX}) \times (\partial I_D/\partial V_G)$, where L and W are the length and width of the channel, respectively, q is the electron charge, and C_{OX} is $\varepsilon_{OX} \times \varepsilon_0/t_{OX}$, which is the gate oxide capacitance per unit area.

Optical Characterization of the PPh_3-Doped WSe_2 Optoelectronic Device: The PPh_3-doped WSe_2 photodetector devices were investigated by performing electrical measurements (I_D–V_G) under both dark and illuminated conditions (Figure S7, Supporting Information). The light source was a dot laser with a wavelength of 520 nm and an optical power of 4.0 mW cm^{-2}. The photoresponsivity (R) was extracted from $R = I_{Photo}/P_{Light}$ where I_{Photo} is the generated photocurrent and P_{Light} is the total incident optical power, and the incident power of the laser was adjusted as 5, 10, 100, and 1000 pW. The photoswitching characteristics of the PPh_3-doped WSe_2 photodetector were investigated under the 520 nm laser illumination, which turned on and off with a cycle of 5 s. The photoresponse times (rising and decaying times) were then extracted between 10% and 90% of the measured maximum photocurrent (I_{max}) data (Figure S4, Supporting Information).

Supporting Information

Supporting Information is available from the Wiley Online Library or from the author.

Acknowledgements

S.-H. J. and D.-H. K. contributed equally to this work. This work was supported by the National Research Foundation of Korea (NRF) funded by the Korean government (MSIP) (Grant No. 2015R1A2A2A01002965).

Received: January 4, 2016
Revised: February 26, 2016

---

[1] B. Radisavljevic, A. Radenovic, J. Brivio, V. Giacornetti, A. Kis, *Nat. Nanotechnol.* **2011**, *6*, 147.
[2] B. Radisavljevic, M. B. Whitwick, A. Kis, *ACS Nano* **2011**, *5*, 9934.

DOI: 10.1002/adma.201600032

[3] E. Zhang, W. Wang, C. Zhang, Y. Jin, G. Zhu, Q. Sun, D. W. Zhang, P. Zhou, F. Xiu, *ACS Nano* **2015**, *9*, 612.

[4] M. Tosun, S. Chuang, H. Fang, A. B. Sachid, M. Hettick, Y. Lin, Y. Zeng, A. Javey, *ACS Nano* **2014**, *8*, 4948.

[5] Z. Yin, H. Li, H. Li, L. Jiang, Y. Shi, Y. Sun, G. Lu, Q. Zhang, X. Chen, H. Zhang, *ACS Nano* **2012**, *6*, 74.

[6] M.-L. Tsai, S.-H. Su, J.-K. Chang, D.-S. Tsai, C.-H. Chen, C.-I. Wu, L.-J. Li, J.-J. Chen, J.-H. He, *ACS Nano* **2014**, *8*, 8317.

[7] S. Jo, N. Ubrig, H. Berger, A. B. Kuzmenko, A. F. Morpurgo, *Nano Lett.* **2014**, *14*, 2019.

[8] G. Fiori, F. Bonaccorso, G. Iannaccone, T. Palacios, D. Neumaier, A. Seabaugh, S. K. Banerjee, L. Colombo, *Nat. Nanotechnol.* **2014**, *9*, 768.

[9] W. Liu, J. Kang, D. Sarkar, Y. Khatami, D. Jena, K. Banerjee, *Nano Lett.* **2013**, *13*, 1983.

[10] O. Salehzadeh, N. H. Tran, X. Liu, I. Shih, Z. Mi, *Nano Lett.* **2014**, *14*, 4125.

[11] M. Massicotte, P. Schmidt, F. Vialla, K. G. Schädler, A. Reserbat-Plantey, K. Watanabe, T. Taniguchi, K. J. Tielrooij, F. H. L. Koppens, *Nat. Nanotechnol.* **2016**, *11*, 42.

[12] X. Hing, J. Kim, S.-F. Shi, Y. Zhang, C. Jin, Y. Sun, S. Tongay, J. Wu, Y. Zhang, F. Wang, *Nat. Nanotechnol.* **2014**, *9*, 682.

[13] C. Gong, L. Colombo, R. M. Wallace, K. Cho, *Nano Lett.* **2014**, *14*, 1714.

[14] J. Kang, W. Liu, D. Sarkar, D. Jena, K. Banerjee, *Phys. Rev. X* **2014**, *4*, 031005.

[15] S. Chuang, C. Battaglia, A. Azcatl, S. McDonnell, J. S. Kang, X. Yin, M. Tosun, R. Kapadia, H. Fang, R. M. Wallace, A. Javey, *Nano Lett.* **2014**, *14*, 1337.

[16] H. Fang, M. Tosun, G. Seol, T. C. Chang, K. Takei, J. Guo, A. Javey, *Nano Lett.* **2013**, *13*, 1991.

[17] L. Yu, A. Zubair, E. J. G. Santos, X. Zhang, Y. Lin, Y. Zhang, T. Palacios, *Nano Lett.* **2015**, *15*, 4928.

[18] P. Tonndorf, R. Schmidt, P. Böttger, X. Zhang, J. Börner, A. Liebig, M. Albrecht, C. Kloc, O. Gordan, D. R. T. Zahn, S. M. de Vasconcellos, R. Bratschitsch, *Opt. Express* **2013**, *21*, 4908.

[19] D.-H. Kang, J. Shim, S. K. Jang, J. Jeon, M. H. Jeon, G. Y. Yeom, W.-S. Jung, Y. H. Jang, S. Lee, J.-H. Park, *ACS Nano* **2015**, *9*, 1099.

[20] C.-H. Chen, C.-L. Wu, J. Pu, M.-H. Chiu, P. Kumar, T. Takenobu, L.-J. Li, *2D Mater.* **2014**, *1*, 034001.

[21] P. Zhao, D. Kiriya, A. Azcatl, C. Zhang, M. Tosun, Y.-S. Liu, M. Hettick, J. S. Kang, S. McDonnell, S. KC, J. Guo, K. Cho, R. M. Wallace, A. Jacey, *ACS Nano* **2014**, *8*, 10808.

[22] B. Mahns, F. Roth, M. Knupfer, *J. Chem. Phys.* **2012**, *136*, 134503.

[23] A. V. Penumatcha, R. B. Salazar, J. Appenzeller, *Nat. Commun.* **2015**, *6*, 8948.

[24] J. D. Lin, C. Han, F. Wang, R. Wang, D. Xiang, S. Qin, X.-A. Zhang, L. Wang, H. Zhang, A. T. S. Wee, W. Chen, *ACS Nano* **2014**, *8*, 5323.

[25] V. Patil, A. Capone, S. Strauf, E.-H. Yang, *Sci. Rep.* **2013**, *3*, 2791.

[26] S. Wang, X. Wang, J. H. Warner, *ACS Nano* **2015**, *9*, 5246.

[27] G.-H. Lee, Y.-J. Yu, X. Cui, N. Petrone, C.-H. Lee, M. S. Choi, D.-Y. Lee, C. Lee, W. J. Yoo, K. Watanabe, T. Tanihuchi, C. Nuckolls, P. Kim, J. Hone, *ACS Nano* **2013**, *7*, 7931.

[28] H.-J. Chuang, X. Tan, N. J. Ghimire, M. M. Perera, B. Chamlagain, M.-C. Cheng, J. Yan, D. Mandrus, D. Tománek, Z. Zhou, *Nano Lett.* **2014**, *14*, 3594.

[29] J. I.-J. Wang, Y. Yang, Y.-A. Chen, K. Watanabe, T. Taniguchi, H. O. H. Churchill, P. Jarillo-Herroero, *Nano Lett.* **2015**, *15*, 1898.

[30] X. Wang, P. Wang, J. Wang, W. Hu, X. Zhou, N. Guo, H. Huang, S. Sun, H. Shen, T. Lin, M. Tang, L. Liao, A. Jiang, J. Sun, X. Meng, X. Chen, W. Lu, J. Chu, *Adv. Mater.* **2015**, *27*, 6575.

[31] S. Liu, X. Yuan, P. Wang, Z.-G. Chen, L. Tang, E. Zhang, C. Zhang, Y. Liu, W. Wang, C. Liu, C. Chen, J. Zou, W. Hu, F. Xiu, *ACS Nano* **2015**, *9*, 8592.

DOI: 10.1002/adma.201600032